# Dual quantum spin Hall insulator by density-tuned correlations in $TaIrTe_4$

Jian Tang,  $^{1,\,*}$  Thomas Siyuan Ding,  $^{1,\,*}$  Hongyu Chen,  $^{2,\,*}$  Anyuan Gao,  $^3$  Tiema Qian,<sup>4</sup> Zumeng Huang,<sup>1</sup> Zhe Sun,<sup>1,3</sup> Xin Han,<sup>5</sup> Alex Strasser,<sup>6</sup> Jiangxu Li,<sup>7,8</sup> Michael Geiwitz, Mohamed Shehabeldin, Vsevolod Belosevich, Zihan Wang, Yiping Wang,<sup>1</sup> Kenji Watanabe,<sup>9</sup> Takashi Taniguchi,<sup>10</sup> David C. Bell,<sup>11</sup> Ziqiang Wang, Liang Fu, 12 Yang Zhang, 7,8 Xiaofeng Qian, 6 Kenneth S. Burch, 1 Youguo Shi,<sup>5</sup> Ni Ni,<sup>4</sup> Guoqing Chang,<sup>2,†</sup> Su-Yang Xu,<sup>3</sup> and Qiong Ma<sup>1,13,†</sup> <sup>1</sup>Department of Physics, Boston College, Chestnut Hill, MA, USA <sup>2</sup>Division of Physics and Applied Physics, School of Physical and Mathematical Sciences, Nanyang Technological University, Singapore <sup>3</sup>Department of Chemistry and Chemical Biology, Harvard University, Cambridge, MA, USA <sup>4</sup>Department of Physics and Astronomy and California NanoSystems Institute, University of California Los Angeles, Los Angeles, CA, USA <sup>5</sup>Beijing National Laboratory for Condensed Matter Physics and Institute of Physics, Chinese Academy of Sciences, Beijing, China <sup>6</sup>Department of Materials Science and Engineering, Texas A&M University, College Station, TX, USA <sup>7</sup>Department of Physics and Astronomy, University of Tennessee, Knoxville, TN, USA <sup>8</sup>Min H. Kao Department of Electrical Engineering and Computer Science, University of Tennessee, Knoxville, Tennessee, USA <sup>9</sup>Research Center for Electronic and Optical Materials, National Institute for Materials Science, Tsukuba, Japan <sup>10</sup>Research Center for Materials Nanoarchitectonics, National Institute for Materials Science, Tsukuba, Japan <sup>11</sup>Harvard John A. Paulson School of Engineering and Applied Sciences and The Center for Nanoscale system, Harvard University, Cambridge, MA, USA <sup>12</sup>Department of Physics, Massachusetts Institute of Technology, Cambridge, MA, USA <sup>13</sup>CIFĂR Ăzrieli Global Scholars program, CIFAR, Toronto, Canada

1

2

10

12

13

15

16

17

18

19

20

21

22

23

25

26

27

28

29

30

31

32

33

<sup>\*</sup> These authors contributed equally.

<sup>†</sup> E-mail: guoqing.chang@ntu.edu.sg; maqa@bc.edu

#### Abstract

The convergence of topology and correlations represents a highly coveted realm in the pursuit of novel quantum states of matter [1]. Introducing electron correlations to a quantum spin Hall (QSH) insulator can lead to the emergence of a fractional topological insulator and other exotic time-reversal-symmetric topological order [2–8], not possible in quantum Hall and Chern insulator systems. In this work, we report a novel dual QSH insulator within the intrinsic monolayer crystal of TaIrTe<sub>4</sub>, arising from the interplay of its single-particle topology and density-tuned electron correlations. At charge neutrality, monolayer TaIrTe<sub>4</sub> demonstrates the QSH insulator, manifesting enhanced nonlocal transport and quantized helical edge conductance. Interestingly, upon introducing electrons from charge neutrality, TaIrTe<sub>4</sub> only shows metallic behavior in a small range of charge densities but quickly goes into a new insulating state, entirely unexpected based on TaIrTe<sub>4</sub>'s single-particle band structure. This insulating state could arise from a strong electronic instability near the van Hove singularities (VHS), likely leading to a charge density wave (CDW). Remarkably, within this correlated insulating gap, we observe a resurgence of the QSH state. Our observation of helical edge conduction in a CDW gap could bridge spin physics and charge orders. The discovery of a dual QSH insulator introduces a new method for creating topological flat minibands via CDW superlattices, which offer a promising platform for exploring time-reversal-symmetric fractional phases and electromagnetism [2-4, 9, 10].

## Introduction

Topology and correlations are two central themes of current condensed matter research [1]. Their interplay gives rise to correlated topological phases, including topological order, which could lead to phenomena such as topological fractionalization, long-range entanglement, and non-Abelian anyons. Recent theory developments have highlighted materials exhibiting both single-particle topological bands and strong correlations as exciting candidates to explore correlated topological phases [11–14]. An intriguing but rarely explored scenario is "QSH + correlations", i.e., to introduce correlations to the  $\mathcal{Z}_2$  band of a QSH insulator. The time-reversal symmetry present for the  $\mathcal{Z}_2$  band can enable time-reversal-symmetric topological order such as the fractional QSH and the helical quantum spin liquid [2–9], unattainable in quantum Hall and Chern insulators [15–19].

Despite the fundamental interest in "QSH + correlations" scenario, it is rarely investigated due to the scarcity of suitable material platforms. First, while the QSH state has been explored in many materials [20–31], achieving the QSH effect with quantized helical edge conduction has been extremely rare [21, 25, 32, 33]. Second, it is even rarer to find a QSH insulator exhibiting strong correlations, as most QSH materials have dispersive bands. One effective way to induce strong correlations involves achieving a large density of states via the VHS (Fig. 1a-b), a strategy that has resurged in recent studies of graphene and kagome materials [34–37]. In this work, we report a new electronic phenomenon that arises from the interplay of QSH topology and VHS-induced correlations, the dual QSH insulator, in a vdW

monolayer crystal TaIrTe<sub>4</sub>. Specifically, we detect two distinct charge gaps: one at charge neutrality point (CNP) and another near the DFT-calculated VHS positions (Fig. 1c). Each gap exhibits QSH helical edge conduction, named as QSH-I and QSH-II, respectively.

#### Lattice and electronic structures

Bulk TaIrTe<sub>4</sub> is a layered (Fig. 1d) Weyl semimetal that has been investigated in both theoretical and experimental studies [38–41]. In contrast, monolayer TaIrTe<sub>4</sub> has not yet been experimentally explored, due to its severe air-sensitivity and the challenges associated with exfoliation. By systematically optimizing the fabrication conditions (Methods), we have successfully accessed the intrinsic electronic properties of monolayer TaIrTe<sub>4</sub> for the first time (see Extended Data Fig. 1 and Supplementary Information (SI) Section 1).

Structurally, monolayer TaIrTe<sub>4</sub> features 1D Ta and Ir chains along the crystalline  $\hat{a}$  axis (Fig. 1e). Within a single unit cell, there are two inequivalent Ta (Ir) chains, which are related by a 180° rotation about the  $\hat{a}$  axis ( $C_{2a}$ ) (Fig. 1e). Observing the b-c plane, the monolayer is made of alternating parallelograms - one parallelogram is formed by two Ta and two Te while the other is formed by two Ir and two Te. In terms of electronic properties, theoretical predictions suggest that monolayer TaIrTe<sub>4</sub> is a QSH insulator with a substantial band gap [42, 43]. Notably, our calculations also reveal prominent VHS close to the single-particle QSH gap, as indicated by the bright intensity spots inside the projected bulk bands in Fig. 1c. We will revisit this lattice and electronic structures, as it proves crucial for understanding our observations.

# 98 Unconventional transport characteristics

We have fabricated high-quality, dual-gated (top gate voltage,  $V_{\rm tg}$  and bottom gate voltage,  $V_{\rm bg}$ ) monolayer TaIrTe<sub>4</sub> devices. We observed highly consistent behaviors across over a dozen devices. Transport characterizations conducted on 19 devices indicate mobility ranging from approximately 10 to 400 cm<sup>2</sup>/(V·s) (SI 1.4). Figure 1f shows the four-probe resistance  $R_{\rm xx}$  as a function of the carrier density n (see electric field E dependence and discussions in SI 4.2 and 5.2). Notably, even for this basic property, monolayer TaIrTe<sub>4</sub> already distinctly differs from known QSH systems [28, 32]. Specifically, in addition to the resistance peak at CNP which is expected based on the single-particle band structure, we observe a second resistance peak in the electron-doped regime at  $\sim 6.5 \times 10^{12}$  cm<sup>-2</sup> (Fig. 1f-g).

# QSH state at charge neutrality

We first study the physics associated with the resistance peak at CNP. As shown in Fig. 2a, the CNP conductance decreases with decreasing temperature and expands into a plateau below 30 K, suggesting a band gap. Also, the conductance saturates at a nonzero value denoted as  $G_0$  in Fig. 2a, hinting at an additional in-gap conduction channel. Importantly, the conductance of this plateau is  $G_0 \sim 72.8 \ \mu\text{S}$ , approaching  $2e^2/h$ . To estimate the magnitude of the band gap, we apply the thermal-activation fit to the temperature-dependent conductance at CNP (with and without subtracting  $G_0$ ) (Fig. 2b). The fitting

yields an activation gap between 20 to 30 meV, which approximately aligns with the first-principles calculated gap at CNP (Fig. 1c).

The finite conductance plateau at the CNP suggests in-gap states, which could arise from edge states or bulk defect states. To gain further insight, we performed nonlocal transport measurements, previously proven effective in studying QSH systems [28, 44] in which significant nonlocal voltage,  $V_{\rm NL}$ , arises from the edge conduction around the outer boundary of the sample (Fig. 2c). In our measurements,  $V_{\rm NL}$  is prominent within the band gap and suppressed outside the gap (Fig. 2d). Moreover, we found negligible  $V_{\rm NL}$  when the edge contribution was eliminated by physically covering the edge with an insulating boron nitride (BN) flake (Extended Data Fig. 5). These observations suggest that the finite conductance plateau in Fig. 2a originates from edge state conduction.

We now study the nature of the edge states (topological or trivial). A defining characteristic of QSH is the quantized conductance of  $2e^2/h$  ( $e^2/h$  per edge) in the short-channel (ballistic) regime [21, 25, 32, 33]. Therefore, we now investigate the edge conduction versus the channel length  $L_{\rm ch}$  via two device designs. In Design-I, a strategy previously utilized in WTe<sub>2</sub> [32], we apply the global top gate to heavily dope the sample and adjust the local bottom gate to neutralize the charge, effectively setting  $L_{\rm ch}$  as the width of the designated local bottom gate (Fig. 2e). In Design-II, the channel is more directly defined between adjacent metal contacts (Fig. 2f). Both designs yielded consistent results in our case: the resistance (conductance) decreases (increases) as  $L_{\rm ch}$  decreases. Upon entering the shortchannel regime, the resistance (conductance) approaches and levels off at the quantized value of  $h/2e^2$  ( $2e^2/h$ ) regardless of the channel width (Fig. 2g). The edge quantization exhibits minimal dependence on current biasing within 100 nA (SI 2.2), suggesting ohmic contacts to the edge channels. The quantization channel length typically ranges from 100 to 200 nm, with our highest-performing sample extending up to 380 nm. Beyond this length, conductance may still saturate to a value on the order of  $2e^2/h$  (Extended Data Fig. 4), implying minimal bulk contribution. This suggests that deviations from quantization are likely due to inelastic edge scattering [45, 46] rather than bulk residual channels.

We conducted further investigations into the magnetic field B dependence of the edge conduction [47, 48]. Our data show that the edge conduction is weakly suppressed by applying perpendicular or in-plane B field (Extended Data Fig. 7). We propose an explanation based on DFT calculation shown in Fig. 1c: the edge Dirac point resides within the valence band of the bulk, making it impossible to position the chemical potential solely within the magnetic gap, leading to a weak magnetic field response (See SI 2.5 for more detailed discussions).

# Insulating state at finite doping

Extrinsically, the resistance peak in the electron-doped regime may be due to disorderinduced localization, while intrinsically, it may arise from the opening of an energy gap at a specific chemical potential due to electron correlations. To explore this further, we present the temperature-dependent conductance across a wider range of carrier densities in Fig. 3a as well as in Extended Data Fig. 3. At n = 0, the temperature dependence displays insulating behavior (Fig. 3b, red curve), consistent with the CNP single-particle gap. As we increase the carrier density to  $n=3.2\times 10^{12}~{\rm cm^{-2}}$ , the temperature dependence becomes metallic (green curve). Further increasing to  $n=6.5\times 10^{12}~{\rm cm^{-2}}$  results in insulating behavior once again (blue curve). In a typical scenario, if disorder played a significant role in inducing insulating behavior at  $n=6.5\times 10^{12}~{\rm cm^{-2}}$ , it should similarly result in insulating behavior at lower carrier densities such as  $n=3.2\times 10^{12}~{\rm cm^{-2}}$ . Figure 3d shows the fitted activation gap  $\Delta$  as a function of carrier density.

We also performed Hall measurements at 60 K. We observed not only the expected sign reversal of the Hall signal at the CNP but also a second sign reversal near the resistive feature at  $6.5 \times 10^{12}$  cm<sup>-2</sup> (Fig. 3e). This additional sign reversal could arise from the emergence of hole-like pockets, consistent with the existence of VHS (Fig. 1c and additional data and analysis in SI 3.1-3.3). Collectively, we propose the following explanation for the double resistance peaks observed in Fig. 1f: The first resistance peak at CNP represents a single-particle gap. Upon electron doping to a certain level, a correlated gap appears from enhanced correlations near the VHS, as illustrated in Fig. 3c.

## A dual QSH insulator

Before moving to more in-depth theoretical considerations, we now explore the topological nature of the emergent insulating state. This is particularly interesting since the new insulating gap occurs at a low filling ( $\sim 6.5 \times 10^{12} \ \rm cm^{-2}$ ) of the QSH conduction band. Our initial findings revealed that the ratio between  $V_{\rm NL}$  and  $V_{\rm L}$  is significant within both the CNP single-particle gap and the second insulating gap while suppressed elsewhere (Fig. 4a-b). This indicates that edge conduction is present within the second gap as well.

To definitively discern if the second insulating state is topological or trivial, we proceeded to measure the conductance of short-channel devices. In Fig. 4c-d, we investigate the temperature-dependent conductance of a fixed short channel length (140 nm) in the vicinity of the second insulating gap. As the temperature decreases, we observe that the conductance stabilizes at a plateau of  $\sim 2e^2/h$ . We further investigate the channel length dependence of the conductance at the second gap. As shown in Fig. 4e, the resistance (conductance) decreases (increases) with decreasing the channel length  $L_{\rm ch}$ . Upon entering the short-channel regime, the resistance (conductance) levels off at the quantized value of  $h/2e^2$  ( $2e^2/h$ ). We also examined the dependence on the magnetic field, which shows a conductance suppression similar to that for the CNP state (SI 4.3). In conclusion, we establish that the second insulating gap also exhibits the QSH state with quantized helical edge conduction.

Beyond the quantized conduction, we have further conducted spin valve experiments [49]. Our results, provided in SI 4.5, indicate that the edge currents within both insulating gaps carry spin. Collectively, we provide strong evidence that monolayer TaIrTe<sub>4</sub> is a novel dual QSH insulator, which consists of two QSH states, both featuring the hallmark helical quantized edge conduction (Fig. 4a).

### Theory of the dual QSH state

We now provide theoretical analyses of this system: First, our first-principles calculations have revealed that the low-energy electronic states primarily originate from the Ta 5d orbitals (see Extended Data Fig. 9 and SI 5.1). The presence of two inequivalent Ta atoms results in two distinct bands, and the fact that they are related by the  $C_{2a}$  symmetry implies that these two bands will exhibit Dirac crossings (see Extended Data Fig. 10). Indeed, our calculations on monolayer TaIrTe<sub>4</sub> show two Dirac cones at the  $\Lambda$  points without spin-orbit coupling (SOC). The inclusion of SOC gaps the Dirac point, giving rise to the single-particle QSH insulating state at CNP (see SI 5.1).

Second, our calculations revealed saddle-point VHS inside the conduction (valence) band. Monolayer TaIrTe<sub>4</sub> has three low-energy Fermi pockets with direct gaps (Fig. 5a) - Two arise from the gapped Dirac cones at  $\Lambda$ , while the third comes from an additional pocket at  $\Gamma$ . As one increases energy, these pockets are found to gradually expand and merge into saddle points in the conduction and valence bands, giving rise to VHS (Figs. 5a-c). Our calculations indicate that achieving the VHS on the hole side requires a higher carrier density. Currently, our data only shows a slight increase in resistance on the hole side, as shown in Fig. 1f.

Third, we attempt to understand the emergent insulating state. Based on the carrier density, the absence of evidence for magnetism, and the value of quantized edge conductance associated with the correlated insulating gap, we identify CDW with translational symmetry breaking as a reasonable state (see detailed discussion in SI 6.1). We computed the electronic charge susceptibility at various wavevectors (Q) via the Lindhard function (Methods). The calculated charge susceptibility shows multiple distinct local maxima at different Q vectors (Fig. 5d). Among these, we identify a specific local maximum at  $Q^* = (0.068\frac{2\pi}{a}, 0\frac{2\pi}{b})$  for the following reasons: (1) It aligns with the 1D Ta chain direction (Fig. 5d left inset). (2) It corresponds to a relatively large supercell spanning 15 atomic unit cells ( $\sim 5.6$  nm), consistent with the low density of the second gap. (3) It connects two adjacent VHS (Fig. 5a) at the energy where the Fermi surface exhibits two parallel contours (3) in Fig. 5c). Subsequently, we computed the folded band structure in the  $Q^*$  defined superlattice (Fig. 5e-f and Methods). Indeed, the introduction of the  $Q^*$  superlattice potential results in the opening of an insulating gap (Fig. 5f), providing a plausible explanation for our experimental data.

Fourth, we continue with the CDW scenario and theoretically evaluate the topology of the CDW gap. As shown in Fig. 5f, we found that the CDW gap indeed hosts nontrivial QSH states by calculating the  $\mathcal{Z}_2$  invariant via the Wilson loop (Methods). Our calculations interestingly show that the nature of the CDW - whether it is topological or trivial - is closely tied to the periodicity of the CDW, as detailed in SI 6.2. The determined  $Q^*$  above leads to a topological CDW whereas larger Q could yield trivial CDW. In contrast, when the CDW periodicity is fixed by  $Q^*$ , the CDW consistently exhibits a topological nature, regardless of the strength of CDW superlattice potential (SI 6.3).

#### Discussions

Our results position TaIrTe<sub>4</sub> as an exemplary system for investigating time-reversal-symmetric (fractionalized) topological states and the interplay between topology and the potential charge order. Employing scanning tunneling microscopy measurements could shed more light on the nature of the correlated state [37]. Furthermore, the emergent insulating state might give rise to the spontaneous breaking of various symmetries (e.g., space-inversion, rotation), which, coupled with the significant Berry curvature of the topological bands, could yield strong second-order nonlinear responses at low frequencies. Additionally, it's worth-while to explore the impact of strain, which could influence the VHS and, consequently, the correlated state.

Our data implies the existence of emergent flat QSH bands: The "QSH" aspect is supported by our observation of quantized edge conduction within the emergent insulating gap; the "flatness" can be inferred from the low carrier density ( $\sim 6.5 \times 10^{12}$  cm<sup>-2</sup>) associated with the emergent gap. The creation of these flat bands, likely originating from the CDW superlattice with a periodicity of a few nanometers, parallels the extensively studied moiré flat bands. In the future, micro-ARPES measurements with gating capabilities would be highly valuable for directly resolving the emergent band structures. Additionally, exploring the fractional filling of these bands at ultralow temperatures in high-quality samples holds significant promise for realizing time-reversal-symmetric fractionalization and topological order [2–10].

#### References

- [1] Tokura, Y. Quantum materials at the crossroads of strong correlation and topology. *Nature Materials* **21**, 971–973 (2022).
- [2] Levin, M. & Stern, A. Fractional topological insulators. *Physical Review Letters* **103**, 196803 (2009).
- [3] Maciejko, J., Qi, X.-L., Karch, A. & Zhang, S.-C. Fractional topological insulators in three dimensions. *Physical Review Letters* **105**, 246809 (2010).
- [4] Santos, L., Neupert, T., Ryu, S., Chamon, C. & Mudry, C. Time-reversal symmetric hierarchy of fractional incompressible liquids. *Physical Review B* **84**, 165138 (2011).
- [5] Goerbig, M. From fractional chern insulators to a fractional quantum spin hall effect. The European Physical Journal B 85, 1–8 (2012).
- [6] Li, W., Sheng, D., Ting, C. & Chen, Y. Fractional quantum spin Hall effect in flat-band checkerboard lattice model. *Physical Review B* **90**, 081102 (2014).
- [7] Wang, C. & Senthil, T. Time-reversal symmetric u(1) quantum spin liquids. *Physical Review X* **6**, 011034 (2016).
- [8] Barkeshli, M., Bonderson, P., Cheng, M. & Wang, Z. Symmetry fractionalization, defects, and gauging of topological phases. *Physical Review B* **100**, 115147 (2019).
- [9] Park, K.-S. & Han, H. Dirac quantization and fractional magnetoelectric effect in interacting topological insulators. *Physical Review B* **82**, 153101 (2010).
- [10] Wang, H.-W., Fu, B., Zou, J.-Y., Hu, Z.-A. & Shen, S.-Q. Fractional electromagnetic response in a three-dimensional chiral anomalous semimetal. *Physical Review B* **106**, 045111 (2022).

- <sup>286</sup> [11] Sheng, D., Gu, Z.-C., Sun, K. & Sheng, L. Fractional quantum Hall effect in the absence of Landau levels. *Nature Communications* **2**, 389 (2011).
- Neupert, T., Santos, L., Chamon, C. & Mudry, C. Fractional quantum Hall states at zero magnetic field. *Physical Review Letters* **106**, 236804 (2011).
- <sup>290</sup> [13] Tang, E., Mei, J.-W. & Wen, X.-G. High-temperature fractional quantum Hall states. <sup>291</sup> Physical Review Letters **106**, 236802 (2011).
- [14] Regnault, N. & Bernevig, B. A. Fractional chern insulator. *Physical Review X*  $\mathbf{1}$ , 021014 (2011).

294

295

- [15] Xie, Y. et al. Fractional chern insulators in magic-angle twisted bilayer graphene. Nature 600, 439–443 (2021).
- <sup>296</sup> [16] Cai, J. et al. Signatures of Fractional Quantum Anomalous Hall States in Twisted MoTe<sub>2</sub>. Nature **622**, 63–68 (2023).
- <sup>298</sup> [17] Zeng, Y. *et al.* Thermodynamic evidence of fractional Chern insulator in moiré MoTe<sub>2</sub>.

  Nature **622**, 69–73 (2023).
- <sup>300</sup> [18] Park, H. *et al.* Observation of Fractionally Quantized Anomalous Hall Effect. *Nature* **622**, 74–79 (2023).
- [19] Xu, F. et al. Observation of integer and fractional quantum anomalous Hall effects in twisted bilayer MoTe<sub>2</sub>. Physical Review X 13, 031037 (2023).
- <sup>304</sup> [20] Bernevig, B. A., Hughes, T. L. & Zhang, S.-C. Quantum spin Hall effect and topological phase transition in HgTe quantum wells. *Science* **314**, 1757–1761 (2006).
- <sup>306</sup> [21] Konig, M. *et al.* Quantum spin Hall insulator state in HgTe quantum wells. *Science* 318, 766–770 (2007).
- Yang, F. et al. Spatial and energy distribution of topological edge states in single Bi(111) bilayer. Physical Review Letters 109, 016801 (2012).
- [23] Xu, Y. et al. Large-gap quantum spin Hall insulators in tin films. Physical Review Letters 111, 136804 (2013).
- <sup>312</sup> [24] Qian, X., Liu, J., Fu, L. & Li, J. Quantum spin Hall effect in two-dimensional transition metal dichalcogenides. *Science* **346**, 1344–1347 (2014).
- <sup>314</sup> [25] Du, L., Knez, I., Sullivan, G. & Du, R.-R. Robust helical edge transport in gated InAs/GaSb bilayers. *Physical Review Letters* **114**, 096802 (2015).
- <sup>316</sup> [26] Zhu, F.-F. *et al.* Epitaxial growth of two-dimensional stanene. *Nature Materials* **14**, 1020–1025 (2015).
- <sup>318</sup> [27] Li, X.-B. *et al.* Experimental observation of topological edge states at the surface step edge of the topological insulator ZrTe<sub>5</sub>. *Physical Review Letters* **116**, 176803 (2016).
- <sup>320</sup> [28] Fei, Z. et al. Edge conduction in monolayer WTe<sub>2</sub>. Nature Physics 13, 677–682 (2017).
- [29] Tang, S. et al. Quantum spin Hall state in monolayer 1T'-WTe<sub>2</sub>. Nature Physics 13, 683–687 (2017).
- [30] Shumiya, N. *et al.* Evidence of a room-temperature quantum spin Hall edge state in a higher-order topological insulator. *Nature Materials* **21**, 1111–1115 (2022).
- Wang, R., Sedrakyan, T. A., Wang, B., Du, L. & Du, R.-R. Excitonic topological order in imbalanced electron-hole bilayers. *Nature* **619**, 57–62 (2023).
- <sup>327</sup> [32] Wu, S. *et al.* Observation of the quantum spin Hall effect up to 100 kelvin in a monolayer crystal. *Science* **359**, 76–79 (2018).
- <sup>329</sup> [33] Zhao, W. *et al.* Realization of the Haldane Chern insulator in a moiré lattice. *Nature* <sup>330</sup> *Physics* 1–6 (2024).
- Wu, S., Zhang, Z., Watanabe, K., Taniguchi, T. & Andrei, E. Y. Chern insulators, van hove singularities and topological flat bands in magic-angle twisted bilayer graphene.

- Nature Materials **20**, 488–494 (2021).
- <sup>334</sup> [35] Zhou, H. *et al.* Isospin magnetism and spin-polarized superconductivity in bernal bilayer graphene. *Science* **375**, 774–778 (2022).
- <sup>336</sup> [36] Yin, J.-X., Lian, B. & Hasan, M. Z. Topological kagome magnets and superconductors. Nature **612**, 647–657 (2022).
- <sup>338</sup> [37] Teng, X. *et al.* Discovery of charge density wave in a kagome lattice antiferromagnet. Nature **609**, 490–495 (2022).
- <sup>340</sup> [38] Ma, J. et al. Nonlinear photoresponse of type-II Weyl semimetals. Nature Materials <sup>341</sup> **18**, 476–481 (2019).
- <sup>342</sup> [39] Belopolski, I. *et al.* Signatures of a time-reversal symmetric Weyl semimetal with only four Weyl points. *Nature Communications* **8**, 942 (2017).
- <sup>344</sup> [40] Cai, S. *et al.* Observation of superconductivity in the pressurized Weyl-semimetal candidate TaIrTe<sub>4</sub>. *Physical Review B* **99**, 020503 (2019).
- Kumar, D. *et al.* Room-temperature nonlinear Hall effect and wireless radiofrequency rectification in Weyl semimetal TaIrTe<sub>4</sub>. *Nature Nanotechnology* **16**, 421–425 (2021).
- [42] Liu, J., Wang, H., Fang, C., Fu, L. & Qian, X. van der Waals stacking-induced topological phase transition in layered ternary transition metal chalcogenides. *Nano Letters* 17, 467–475 (2017).
- Guo, P.-J., Lu, X.-Q., Ji, W., Liu, K. & Lu, Z.-Y. Quantum spin Hall effect in monolayer and bilayer TaIrTe<sub>4</sub>. *Physical Review B* **102**, 041109 (2020).
- Roth, A. et al. Nonlocal transport in the quantum spin Hall state. Science **325**, 294–297 (2009).
- <sup>355</sup> [45] Xu, C. & Moore, J. E. Stability of the quantum spin Hall effect: Effects of interactions, disorder, and  $\mathcal{Z}_2$  topology. *Physical Review B* **73**, 045322 (2006).
- Maciejko, J. et al. Kondo effect in the helical edge liquid of the quantum spin Hall state. Physical Review Letters 102, 256803 (2009).
- <sup>359</sup> [47] Zhang, S.-B., Zhang, Y.-Y. & Shen, S.-Q. Robustness of quantum spin Hall effect in an external magnetic field. *Physical Review B* **90**, 115305 (2014).
- [48] Ma, E. Y. *et al.* Unexpected edge conduction in mercury telluride quantum wells under broken time-reversal symmetry. *Nature Communications* **6**, 7252 (2015).
- <sup>363</sup> [49] Li, C. *et al.* Electrical detection of charge-current-induced spin polarization due to spin-momentum locking in Bi<sub>2</sub>Se<sub>3</sub>. *Nature Nanotechnology* **9**, 218–224 (2014).

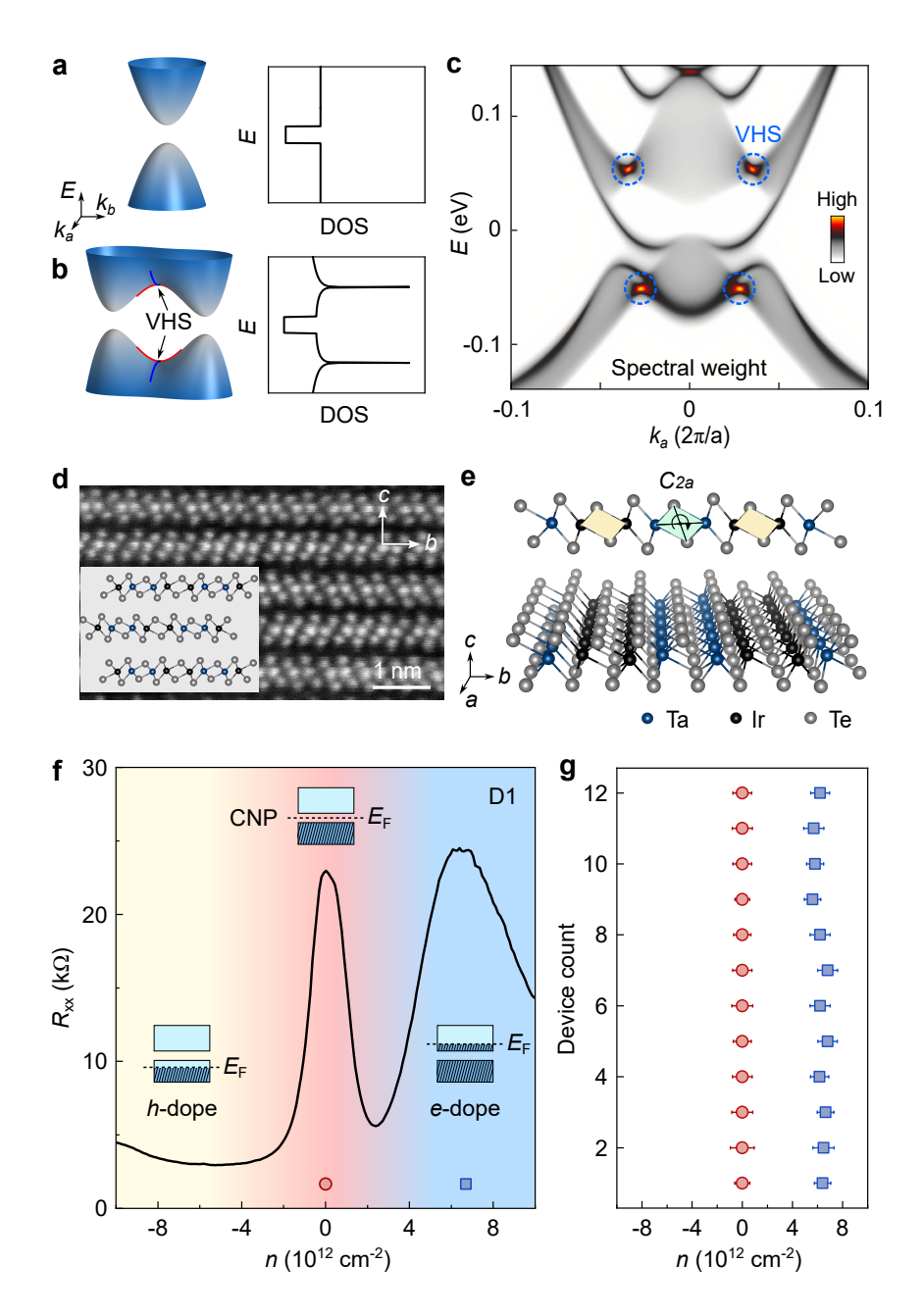


Figure 1: Electronic band structure, lattice structure, and basic electrical characterization of monolayer TaIrTe<sub>4</sub>. a, Sketch of a simple parabolic band structure featuring constant density of states (DOS) beyond the band gap. b, Sketch of two parabolic bands merging to form van Hove singularity (VHS), leading to divergent DOS. c, First-principles calculated projected spectral weight along the  $k_a$  direction showing the edge state dispersion and bulk VHS. d, Cross-sectional TEM image of the TaIrTe<sub>4</sub> crystal. The inset illustrates the overlap with the atomic configuration of TaIrTe<sub>4</sub>. e, Lattice structure and symmetry of monolayer TaIrTe<sub>4</sub>. f, The typical four probe resistance  $R_{xx}$  versus carrier density n at T = 1.7 K (device D1). The light yellow (blue) shaded region indicates the point at which resistance begins to increase in the hole (electron)-doped regions, respectively. g, A summary of the resistance peak positions across a dozen of devices. The error bars are determined based on the point at which the resistance decreases to 95 % of the peak value.

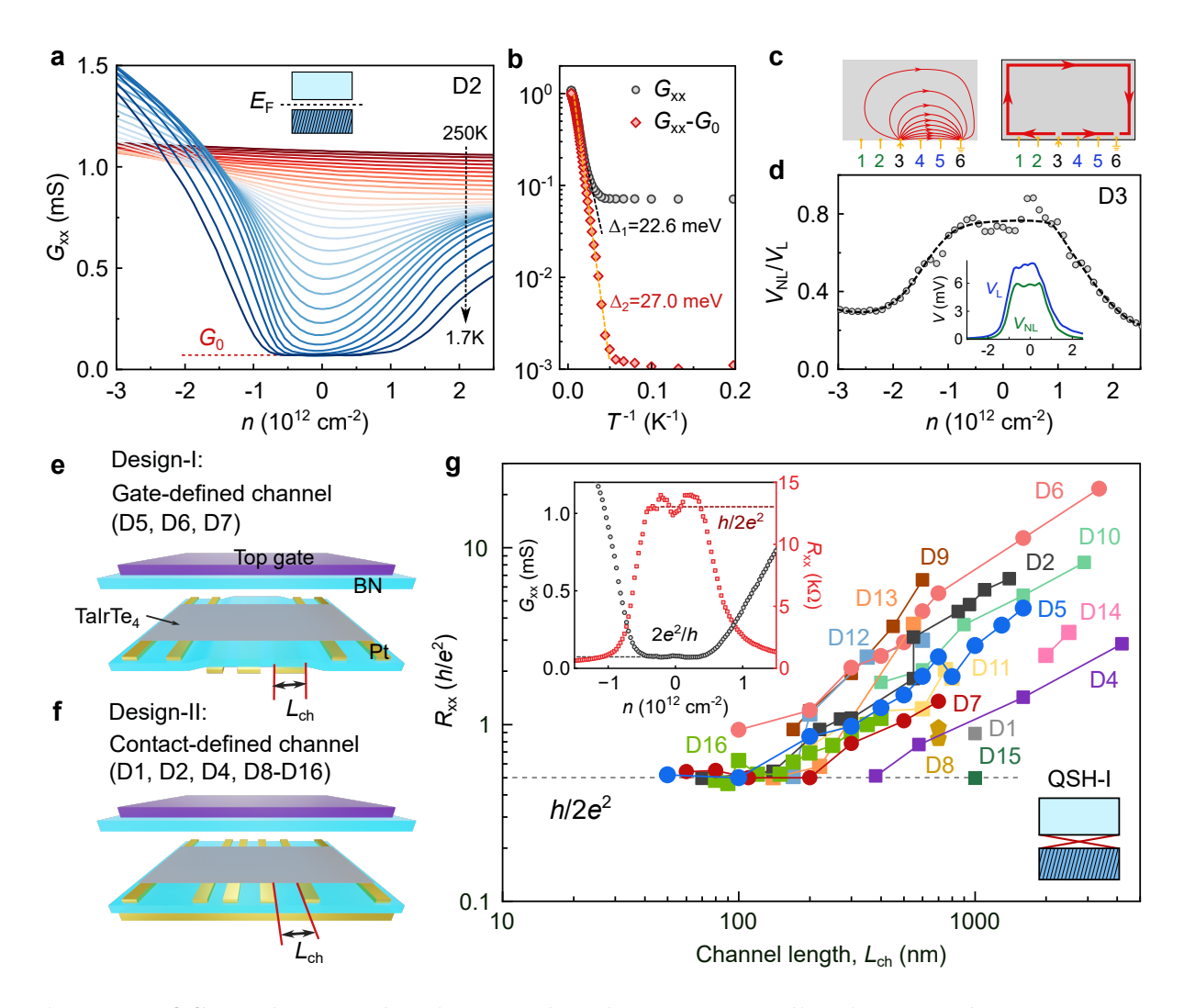


Figure 2: QSH edge conduction at the charge neutrality in monolayer TaIrTe<sub>4</sub>. a, The four-probe conductance  $G_{xx}$  of device D2 with a channel length  $L_{ch} = 140$  nm at different temperatures.  $G_{xx}$  plateaued to a constant value  $G_0$  at the charge neutrality at low temperatures. b, The band gap  $\Delta$  is extracted to be  $\sim 22.6$  meV (without subtracting  $G_0$ ) and  $\sim 27.0$  meV (subtracting  $G_0$ ), determined from the Arrhenius fitting  $G_{xx}(T) \propto$  $\exp(-\Delta/2k_{\rm B}T)$ . c, Schematic of current distribution based on bulk (left) and edge (right) contributions. The bulk (ohmic) contribution results in a weak nonlocal response, while the edge contribution leads to a significant nonlocal voltage drop. d, The ratio between nonlocal and local voltages  $V_{\rm NL}/V_{\rm L}$  is large inside the CNP gap measured with device D3  $(L_{\rm ch}=1~\mu{\rm m}, {\rm also see} {\rm Extended} {\rm Data} {\rm Fig.} {\rm 5}).$  e-f, Schematic illustrations of two kinds of short-channel devices: gate-defined channel with  $L_{\rm ch}$  determined by the gate width (e) and contact-defined channel with  $L_{\rm ch}$  determined by the distance between two adjacent contacts (f). g, Channel length dependence of the plateau resistance at CNP. The resistance reaches  $h/2e^2$  for  $L_{\rm ch} \leq 100$  nm in devices D2 and D5,  $L_{\rm ch} \leq 200$  nm in device D7,  $L_{\rm ch} = 380$  nm (inset) in device D4, and  $L_{\rm ch} \leq 150$  nm in device D16. For clarity, individual curves for D2, D5, D7, D16 are shown in Extended Data Fig. 6. More data related to panel g can be found in SI 4.1.

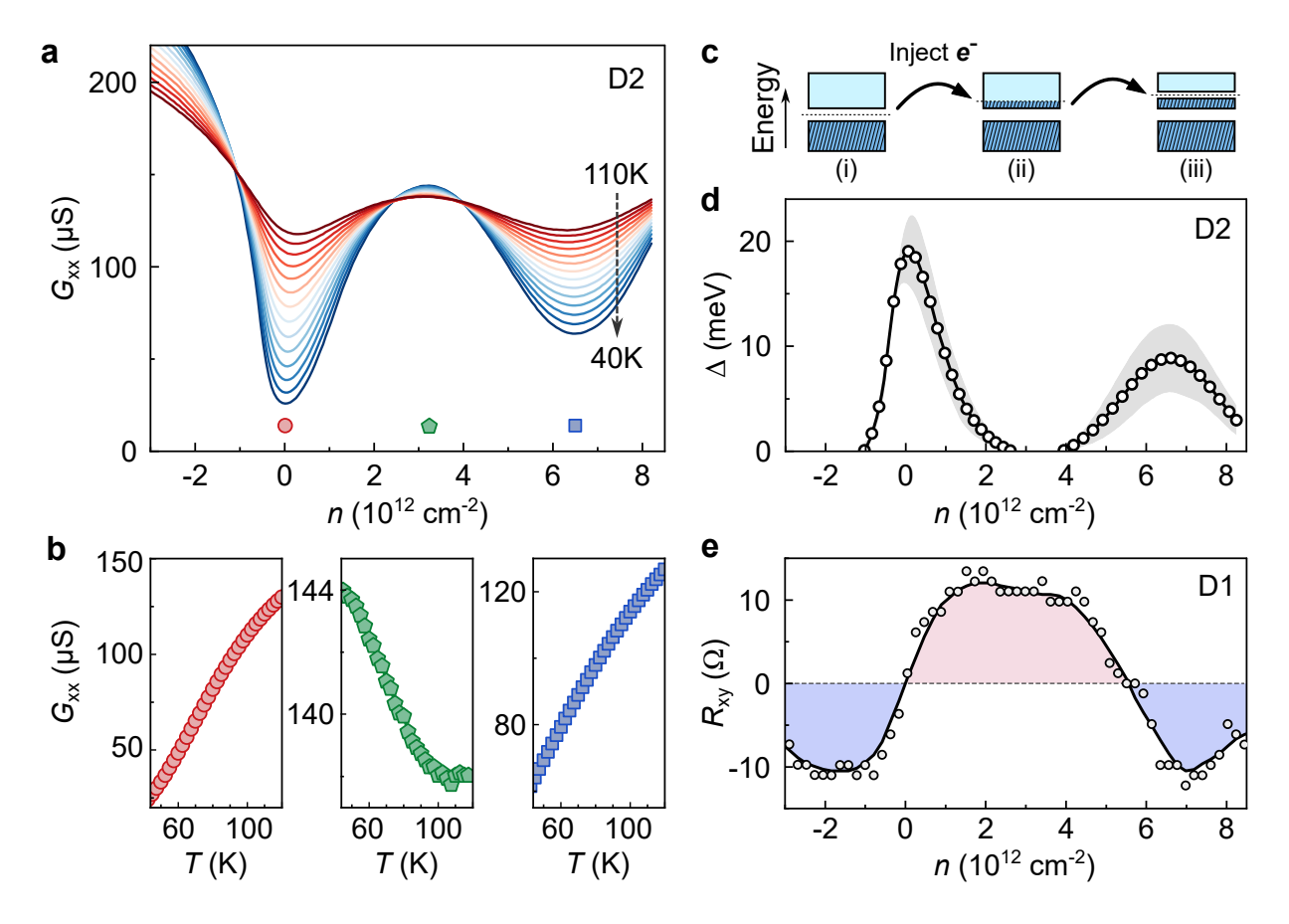


Figure 3: Emergent insulating state at finite doping. a, The temperature-dependent four probe conductance  $G_{xx}$  versus carrier density n across a temperature range from 110 K to 40 K (device D2,  $L_{ch} = 550$  nm). b, Temperature dependence behavior at three representative carrier densities. The colors of the data points in (b) correspond to the carrier densities marked in (a). c, Sketch of a scenario of correlation-induced gap opening at finite doping. d, The size of the fitted activation gap versus n. The shaded region in grey delineates the error bounds associated with the energy gap fits. e, The anti-symmetrized Hall resistance  $R_{xy}$  versus n at B = 5 T and T = 60 K (see SI 3.1 for details).

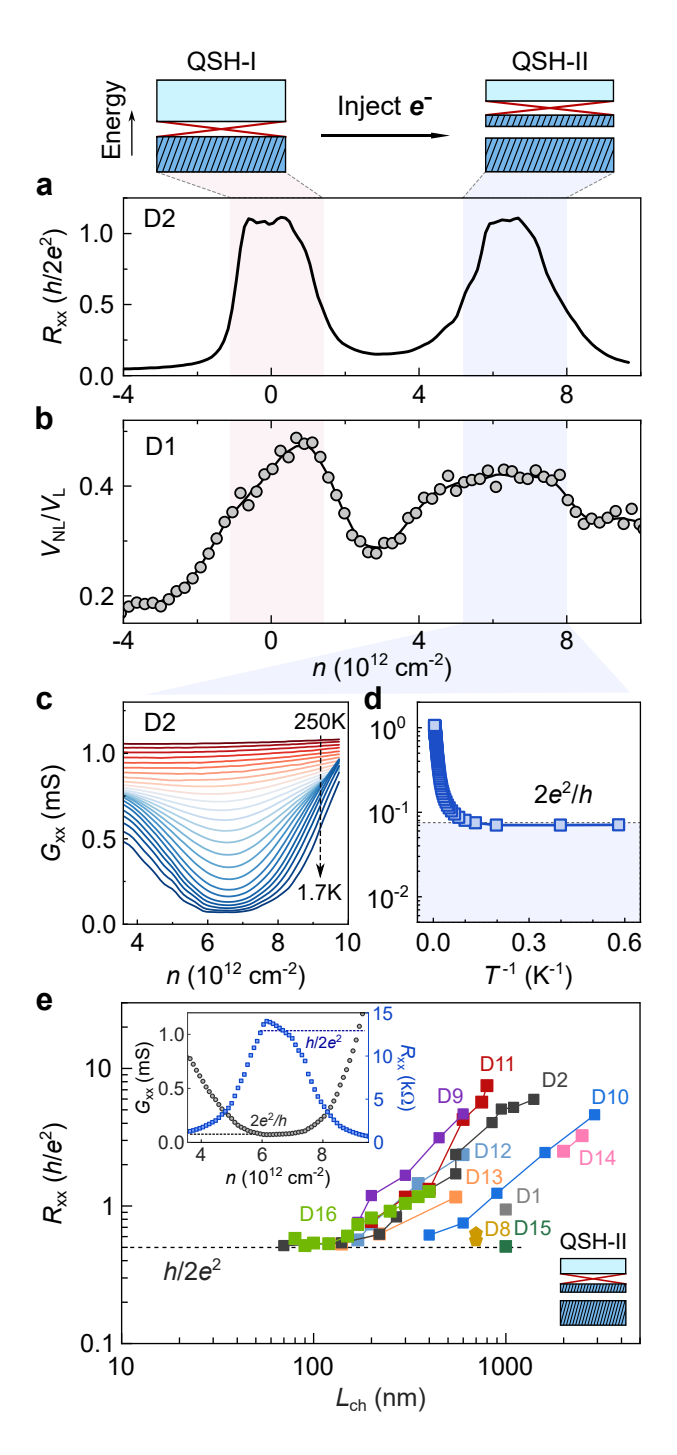


Figure 4: The dual quantum spin hall (dual-QSH) effect in monolayer TaIrTe<sub>4</sub>. a, Resistance versus carrier density (D2,  $L_{\rm ch} = 140$  nm) at T = 1.7 K and the schematic of the dual-QSH. Two resistance plateaus are developed at CNP and  $n \sim 6.5 \times 10^{12}$  cm<sup>-2</sup>, corresponding to the QSH-I and QSH-II states, respectively. b, The ratio between nonlocal and local voltages ( $V_{\rm NL}/V_{\rm L}$ ) has two maxima around the CNP and  $n \sim 6.5 \times 10^{12}$  cm<sup>-2</sup> (measured in device D1,  $L_{\rm ch} = 1~\mu{\rm m}$ , also see Extended Data Fig. 8). c, Conductance versus n around the emergent insulating gap (D2,  $L_{\rm ch} = 140$  nm). d, The minimum conductance in (c) versus temperature ( $T^{-1}$ ), which plateaus at  $\sim 2e^2/h$  at low temperatures. e, Channel length dependence of the resistance at the emergent gap. The resistance approaches  $\sim h/2e^2$  for  $L_{\rm ch} \leq 140$  nm in device D2, and  $L_{\rm ch} \leq 120$  nm in device D16. For clarity, individual curves for D2, D16 are shown in Extended Data Fig. 6 with more data in SI 4.1.

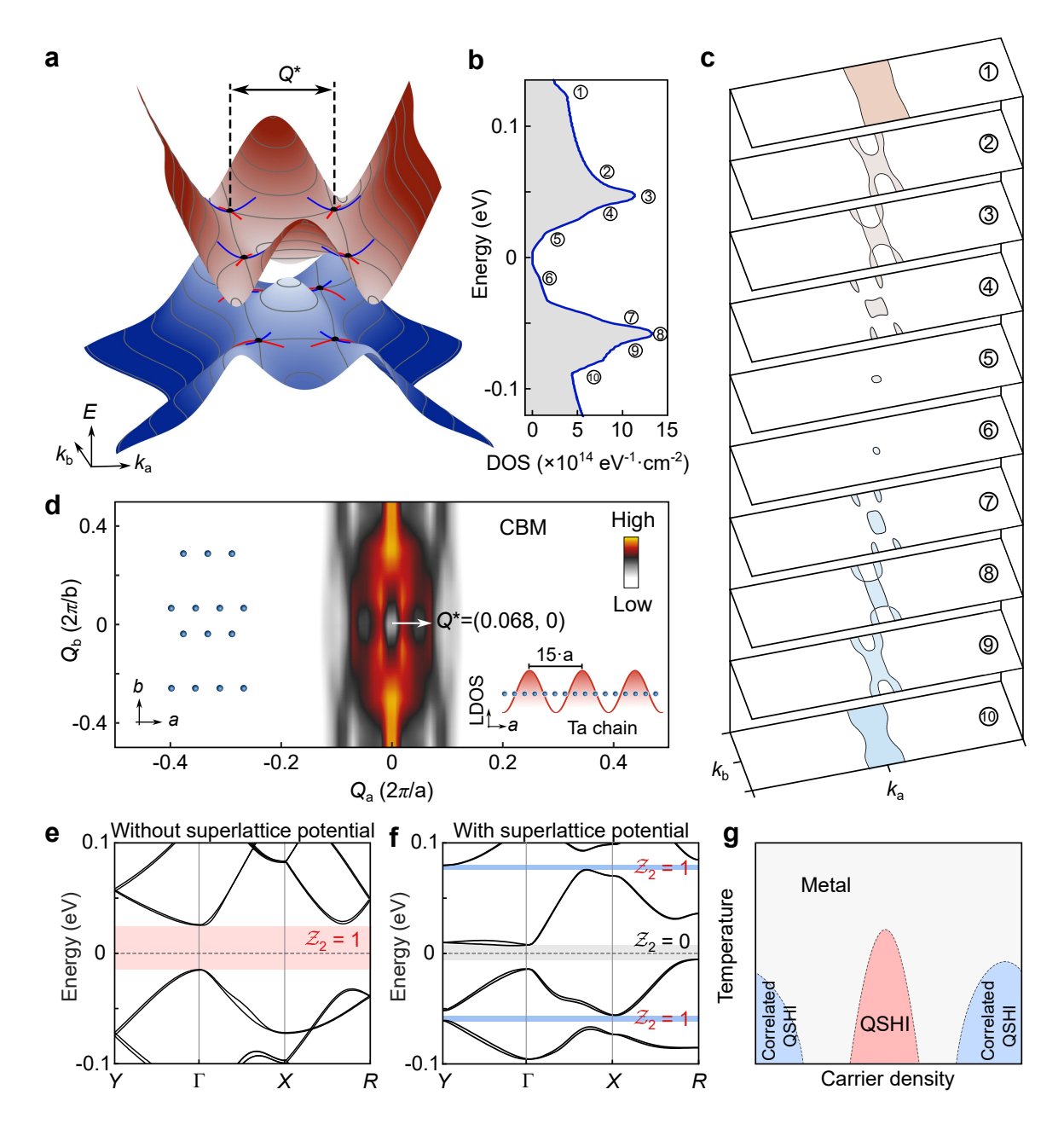


Figure 5: Theoretical investigation of the dual QSH state in monolayer TaIrTe<sub>4</sub>. a, The band structure of monolayer TaIrTe<sub>4</sub> with VHS denoted by black dots. b, The calculated DOS as a function of energy. c, The constant energy contours at different energies, numbered from ① to ①. Their energy values can be found in panel (b). d, Calculated electronic susceptibility of the conduction band based on the first-principles band structure. The white arrow highlights a local maximum of the electronic susceptibility at a wavevector  $Q^*$ .  $Q^*$  connects two neighboring VHS along the  $k_a$  direction as marked in (a), which corresponds a superlattice of  $\sim 15$  unit cells alone the 1D chain direction (see right inset). The left inset shows the atomic structure of TaIrTe<sub>4</sub> with Ta chains highlighted. The same calculation for the valence band can be found in SI 5.5. e-f, The folded band structure with a superlattice periodicity of 15 unit cells, (e) without superlattice potential, and (f) with superlattice potential. g, Conjectured phase diagram of monolayer TaIrTe<sub>4</sub>.

#### Methods

TaIrTe<sub>4</sub> crystal growth: TaIrTe<sub>4</sub> crystals were synthesized by a solution-growth method with Te flux. High-purity (> 99.99%) Ta, Ir, and Te elements were mixed at a molar ratio of 3:3:94 in an alumina crucible and sealed in a vacuum quartz tube. The quartz tube was slowly heated up to 1373 K, maintained for 10 hours and then gradually cooled down to 873 K at a rate of 2 K/h. The shiny, needle-like single crystals were separated from the Te flux by centrifuging. The TaIrTe<sub>4</sub> single crystals were characterized by atomic-resolution cross-sectional scanning transmission electron microscopy (STEM), selected area electron diffraction (SAED), energy-dispersive X-ray spectroscopy (EDS) and residual resistivity ratio (RRR) for crystalline properties, atomic structure, elemental ratio, and sample electrical quality (see detailed characterizations in SI 1.1-1.2).

Mechanical exfoliation and layer number identification of TaIrTe<sub>4</sub>: The TaIrTe<sub>4</sub> were exfoliated on Si/SiO<sub>2</sub> substrates (SiO<sub>2</sub> is 285 nm thickness) by the Scotch tape method. To address the air-sensitive nature of thin TaIrTe<sub>4</sub> flakes, the exfoliation and the following device fabrication processes were performed in an argon-glovebox. We introduced gentle oxygen plasma treatment and heating process to increase the exfoliation yield. Prior to the exfoliation process, we employed a mild oxygen plasma treatment using the Anatech Barrel plasma cleaning system. The treatment involved a flow rate of 40 sccm at a power setting of 100 W for 10 minutes to clean the Si/SiO<sub>2</sub> substrate. Subsequently, we placed the Si/SiO<sub>2</sub> substrates onto the TaIrTe<sub>4</sub> tape, carefully pressing the stack to eliminate any trapped air bubbles. The tape (with Si/SiO<sub>2</sub> substrates) was then heated on a hot plate at a temperature of 80°C for 10 minutes. Finally, we carefully removed the substrates from the TaIrTe<sub>4</sub> tape and inspected them for the presence of thin flakes using an optical microscope.

We used multiple characterizations to determine the layer number of TaIrTe<sub>4</sub> flakes as shown in Extended Data Fig. **1**, including optical contrast, atomic force microscopy (AFM), Raman spectroscopy [50], and cross-sectional STEM. Extended Data Fig. **1a** displays optical images of representative TaIrTe<sub>4</sub> flakes situated on a SiO<sub>2</sub> substrate, revealing distinct optical contrast variations corresponding to different layer numbers. The quantitative relationship between optical contrast ( $C = \frac{I_{\text{flake}} - I_{\text{substrate}}}{I_{\text{flake}} + I_{\text{substrate}}}$ ) and layer numbers can be found in SI 1.2. Extended Data Fig. **1b** displays the surface morphology of exfoliated TaIrTe<sub>4</sub> flakes, examined using a Park NX10 atomic force microscopy (AFM) system in tapping mode with an NCHR tip. The height linecut (inset) reveals a step of approximately 0.8 nm, indicative of a monolayer thickness [51]. Raman spectroscopy also exhibits layer-dependent behavior (Extended Data Fig. **1c**): with increasing layer numbers, the intensity ratio of A<sub>2</sub> (@125.7 cm<sup>-1</sup> for 1L)/A<sub>2</sub> (@137.3 cm<sup>-1</sup> for 1L) rises, and the A<sub>1</sub> mode (@231.8 cm<sup>-1</sup> for 1L) shifts toward lower wavenumbers. Additionally, cross-sectional STEM results in Extended Data Fig. **1d** directly confirm the layer numbers (layer thickness approximately 0.7 nm, consistent with AFM results). These diverse characterization methods, collectively, and unambiguously determine layer numbers.

**Device fabrication and measurements:** Because of the air-sensitivity of thin TaIrTe<sub>4</sub> flakes, we adopted the bottom contact structure with BN encapsulation. The metal electrodes (both gates and contacts) were patterned by standard UV or e-beam lithography via the Heidelberg  $\mu$ PG101 laser writing and the Elionix HS50 e-beam writing systems. Metal

electrodes, consisting of 2 nm Ti and 10 nm Pt layers, were deposited using an e-beam evaporator (Angstrom Engineering) and subsequently annealed in a tube furnace at 350°C for 3 hours in an Ar/H<sub>2</sub> (1:1) forming gas atmosphere. The metal electrodes were fabricated under ambient conditions and subsequently transferred into a glovebox for further processing. Within the glovebox, we conducted the assembly of the BN/few-layer graphene stack (for the top gate structure), as well as the exfoliation, identification, stacking, and encapsulation of TaIrTe<sub>4</sub> flakes. This glovebox is equipped with a dry transfer stage and an optical microscope to facilitate these operations. For a detailed fabrication process, please refer to Extended Data Fig. 2 and SI 1.3. To safeguard the final device, we applied a PMMA capping layer via spin coating while still within the glovebox.

Electrical transport measurements were conducted using a variety of cryogenic systems, including the Montana cryostat, Quantum Design Opticool, PPMS, and MPMS3 systems. Standard lock-in techniques were predominantly employed to measure most of the electrical signals. Gate voltages were applied using Keithley source meters. In dual-gated devices, the charge carrier densities (n) and the external electric field (D) can be independently adjusted through the combination of the top gate voltage  $(V_{tg})$  and the bottom gate voltage  $(V_{bg})$ .

$$n = \frac{\epsilon_0 \epsilon_{\rm BN} V_{\rm bg}}{e d_{\rm b}} + \frac{\epsilon_0 \epsilon_{\rm BN} V_{\rm tg}}{e d_{\rm t}},\tag{1}$$

$$D = \frac{1}{2} \left( \frac{\epsilon_0 \epsilon_{\rm BN} V_{\rm bg}}{d_{\rm b}} - \frac{\epsilon_0 \epsilon_{\rm BN} V_{\rm tg}}{d_{\rm t}} \right), \tag{2}$$

Here,  $\epsilon_0$  is the vacuum permittivity,  $\epsilon_{\rm BN}$  is the BN dielectric constant ( $\epsilon_{\rm BN} \approx 3$ ) and  $d_{\rm b}(d_{\rm t})$  is the thickness of the bottom (top) BN dielectric.

First-principles calculations: The electronic structures of TaIrTe<sub>4</sub> were calculated from density functional theory via the Vienna ab-initio simulation package (VASP) [52]. The exchange correlation functional was considered by the generalized gradient approximation (GGA) [53]. The energy cutoff of plane waves was set to be 500 eV and the smearing width of the Gaussian smearing method was chosen to be 0.05 eV. A Gamma-centered k mesh  $(16 \times 8 \times 1)$  was used for the BZ integrations. To get the ground state, the convergence criteria of lattice optimizations were set to  $10^{-6}$  eV and 0.1 meV/ Å for the total energy and ionic forces, respectively. The optB88-vdW correlation functional [54] was used to describe the vdW interactions for 2D materials. The obtained Bloch wavefunctions were projected onto Wannier functions via using the WANNIER90 package [55]. The density functional perturbation theory implemented in VASP was performed to obtain the force constants with a  $3 \times 2 \times 1$  supercell for phonon dispersion by Phonopy code [56]. The real space Hamiltonian  $H_r$  was constructed by s and d orbitals of Ta, p orbital of Te, s and d orbitals of Ir. The edge states were calculated by iterating the surface Green function [57]. The electronic susceptibility  $\chi(q)$  was calculated by the Lindhard function:

$$\chi(q) = \sum_{k} \frac{f_k(1 - f_{k+q})}{\varepsilon_{k+q} - \varepsilon_k + i\Gamma}$$
(3)

where f is the Fermi Dirac distribution,  $\varepsilon$  is the momentum-dependence energy and  $\Gamma$  is the broadening. The CDW modulation of electronic structure was performed by the Fröhlich-

Peierls model [58]:

$$H = H_r + V\cos(Q \cdot x)\psi_r^{\dagger}\psi_r \tag{4}$$

where V is the modulation strength and only the intra-orbital interaction is considered. The periodicity of potential was determined by the  $Q^*$  vector denoted in Fig. 5d.

To figure out the origin of the topology of the band with superlattice potential, we perform calculations of bands and Wilson loop with continuously changed periodicity based on an eight-band tight-binding model. The eight-band tight-binding model is fitted by WANNIER90 package [55] and constructed by two Ta's  $d_{xz}$ -orbital and two Te's  $p_z$ -orbital with spin-up, down components and spin-orbit coupling. We confirmed that our eight-band tight-binding model captures the same saddle points and helical edge as the tight-binding model with full orbitals.

#### References

- [50] Liu, Y. et al. Raman signatures of broken inversion symmetry and in-plane anisotropy in type-II Weyl semimetal candidate TaIrTe<sub>4</sub>. Advanced Materials **30**, 1706402 (2018).
- [51] Dong, X. et al. Observation of topological edge states at the step edges on the surface of type-II Weyl semimetal TaIrTe<sub>4</sub>. ACS Nano 13, 9571–9577 (2019).
  - [52] Kresse, G. & Furthmüller, J. Efficient iterative schemes for ab initio total-energy calculations using a plane-wave basis set. *Physical Review B* **54**, 11169 (1996).
- [53] Perdew, J. P., Burke, K. & Ernzerhof, M. Generalized gradient approximation made simple. *Physical Review Letters* **77**, 3865 (1996).
- [54] Klimeš, J., Bowler, D. R. & Michaelides, A. Van der Waals density functionals applied to solids. *Physical Review B* **83**, 195131 (2011).
- <sup>472</sup> [55] Mostofi, A. A. *et al.* wannier90: A tool for obtaining maximally-localised Wannier functions. *Computer Physics Communications* **178**, 685–699 (2008).
- <sup>474</sup> [56] Togo, A. & Tanaka, I. First principles phonon calculations in materials science. *Scripta Materialia* **108**, 1–5 (2015).
- Bryant, G. W. Surface states of ternary semiconductor alloys: effect of alloy fluctuations in one-dimensional models with realistic atoms. *Physical Review B* **31**, 5166 (1985).
- [58] Fröhlich, H. On the theory of superconductivity: The one-dimensional case. *Proceedings*of the Royal Society of London. Series A. Mathematical and Physical Sciences **223**,
  296–305 (1954).

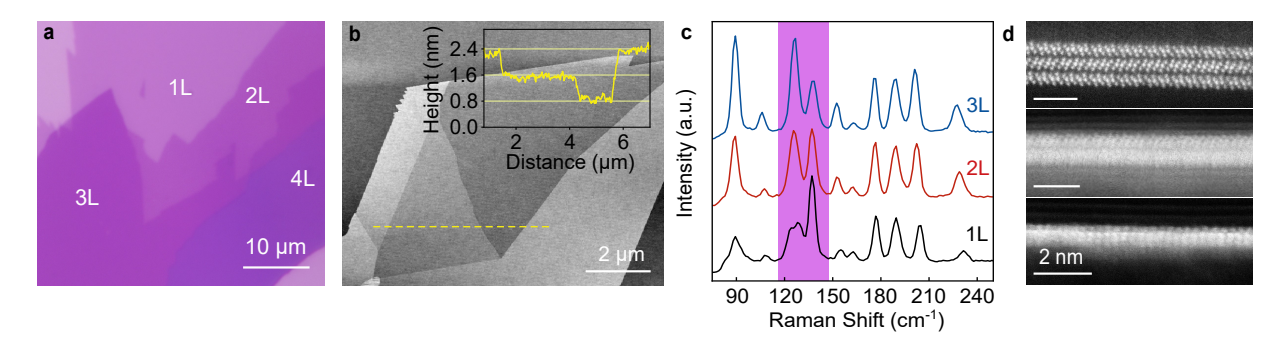
Acknowledgements: We thank Jennifer Cano, Valla Fatemi, Rafael Fernando, Luqiao Liu, Haizhou Lu, Xiao-Bin Qiang, Ying Ran, Brian Skinner, Aviram Uri, Ilija Zeljkovic, Fan Zhang, and Yi Zhang for fruitful discussions. Q.M. acknowledges support from the Air Force Office of Scientific Research grant FA9550-22-1-0270 (transport measurements and data analysis). Q.M. and S.-Y.X. acknowledge support from the Center for the Advancement of Topological Semimetals, an Energy Frontier Research Center funded by the US Department of Energy Office of Science, through the Ames Laboratory under contract DEAC02-07CH11358 (device fabrication). Q.M. also acknowledges support from the National Science Foundation (NSF) CAREER award DMR-2143426 (manuscript writing), the Canadian Institute for Advanced Research (CIFAR) Azrieli Global Scholar Program and the

Alfred P. Sloan Foundation. G.C. acknowledges support from the National Research Foundation, Singapore under its Fellowship Award (NRF-NRFF13-2021-0010) and the Nanyang Assistant Professorship grant. N.N. acknowledges support from the US Department of Energy, Office of Science, under award number DE-SC0021117 (single-crystal growth and characterization of TaIrTe4). Y.S. acknowledges support from the Strategic Priority Research Program of the Chinese Academy of Sciences (grant number XDB33030000) and the Informatization Plan of the Chinese Academy of Sciences (CAS-WX2021SF-0102). K.S.B. and Y.W. acknowledge support from the Air Force Office of Scientific Research under award number FA9550-20-1-0246. X.Q. acknowledges support from the NSF under award number DMR-1753054 and from the donors of the American Chemical Society Petroleum Research Fund under grant number 65502-ND10. D.C.B. acknowledges support from the Harvard University Center for Nanoscale Systems, a member of the National Nanotechnology Coordinated Infrastructure Network, under NSF award number ECCS-2025158, and the STC Center for Integrated Quantum Materials, NSF grant number DMR-1231319. Z.S. acknowledges support from Swiss National Science Foundation under grant number P500PT-206914. M.G. acknowledges the support of the NSF Electronics, Photonics and Magnetic Devices programme through grant 2211334. A.S. acknowledges support from DMR-2103842. Portions of this research were conducted with the advanced computing resources provided by Texas A&M High Performance Research Computing. J.L. and Y.Z. are partly supported by the NSF Materials Research Science and Engineering Center programme through the UT Knoxville Center for Advanced Materials and Manufacturing (grant number DMR-2309083). L.F. and Q.M. acknowledge support from the National Science Foundation Convergence Program under grant number ITE-2235945. Ziqiang Wang is supported by the US Department of Energy, Basic Energy Sciences grant number DE-FG02-99ER45747. K.W. and T.T. acknowledge support from the Japan Society for the Promotion of Science KAKENHI (grant numbers 21H05233 and 23H02052) and World Premier International Research Center Initiative, MEXT, Japan. We also acknowledge that some of the work was carried out in the Boston College cleanroom and nanotechnology facilities.

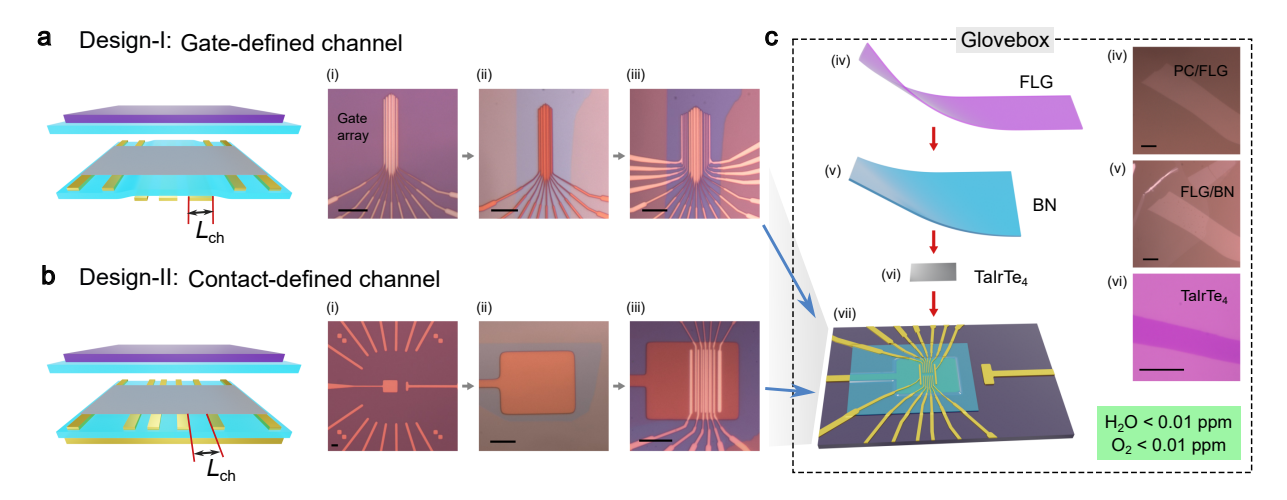
Author contributions: Q.M. conceived the experiments and supervised the project. J.T. fabricated the devices with the help of T.S.D., A.G., M.G., S.-Y.X., and K.S.B. J.T. performed the electrical measurements, and analyzed data with the assistance from T.S.D, A.G., Z.H., Z.S. M.S., V.B. and Z.H.W. A.S. and X.Q. performed the first-principles calculations of the single-particle band; H.C. and G.C. performed the calculations for different edge terminations, electronic susceptibility, CDW band structures, and topology; J.L. and Y.Z. performed the phonon dispersion calculation. L.F. and Z.Q.W. supplied the theory inputs. Y.W. and K.S.B. performed the Raman measurements. D.C.B. carried out the TEM characterization. T.Q., X.H., Y.S., and N.N. grew the TaIrTe<sub>4</sub> bulk crystals. K.W. and T.T. grew the BN bulk crystals. Q.M., S.-Y.X., and J.T. wrote the manuscript with input from all authors.

Competing interests: The authors declare that they have no competing interests.

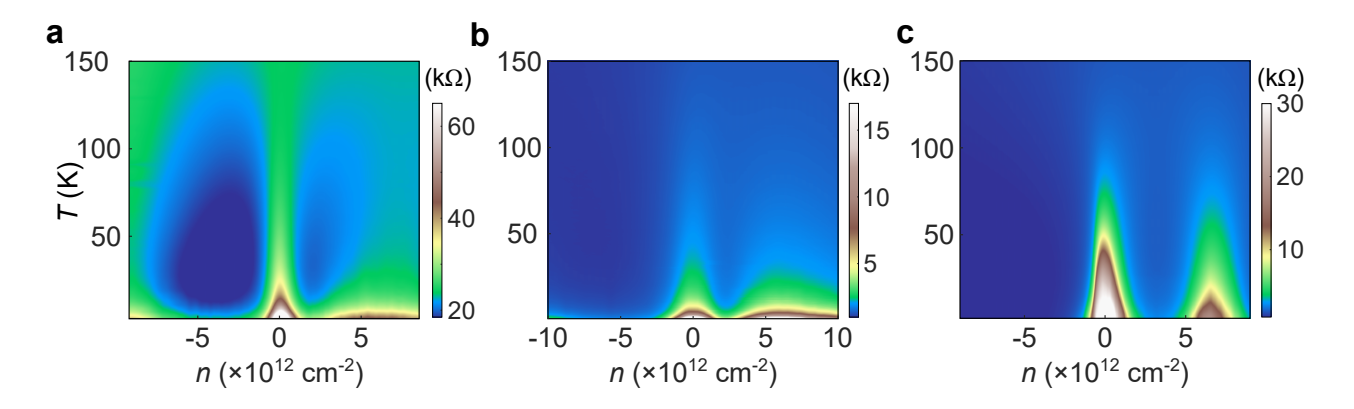
**Data availability:** Source data are provided with this paper. All other data that support the plots within this paper and other findings of this study are available from the corresponding authors upon reasonable request.



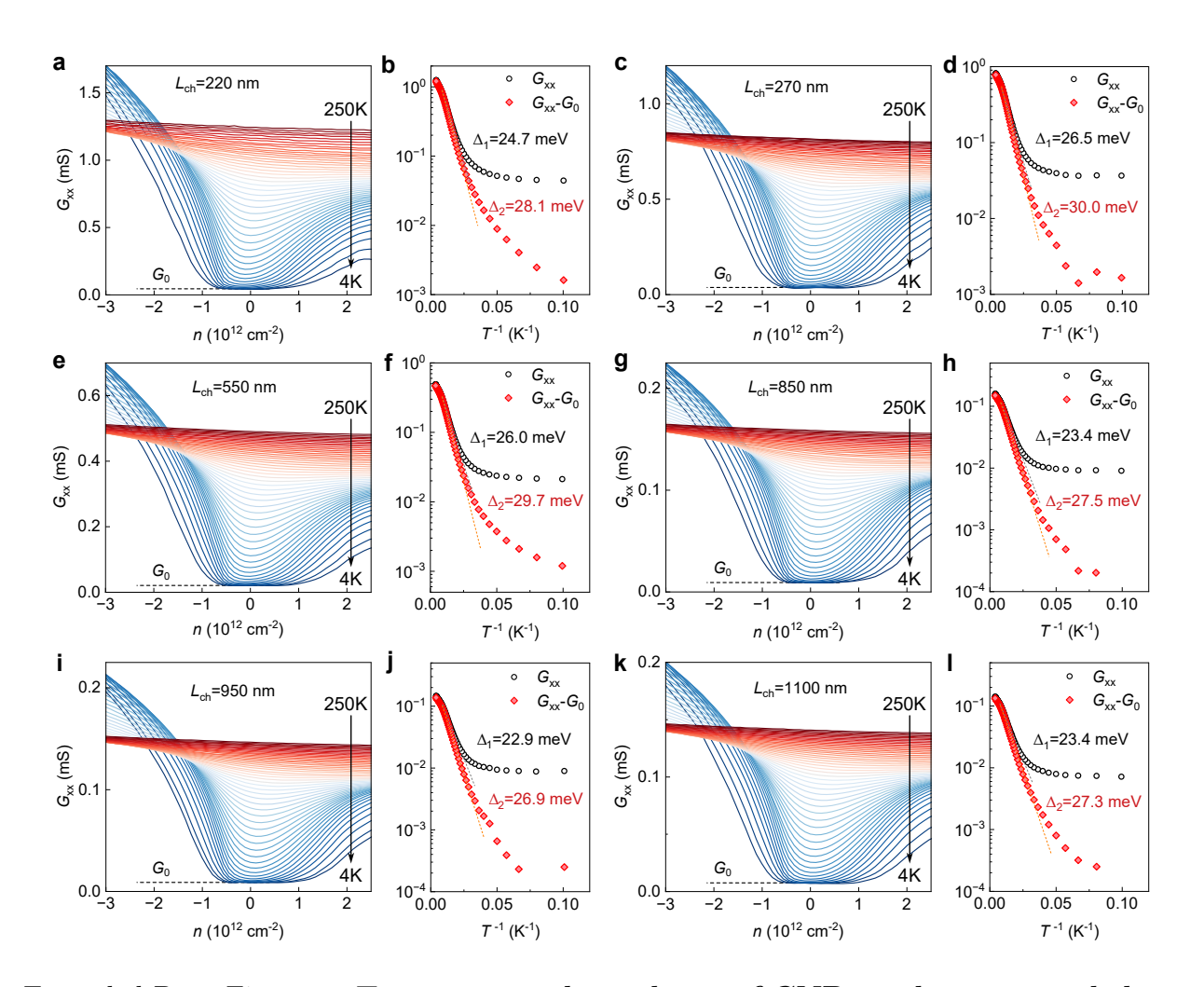
Extended Data Figure 1: Basic characterizations of TaIrTe<sub>4</sub> flakes. a, Optical image displaying exfoliated TaIrTe<sub>4</sub> flakes on a Si/SiO<sub>2</sub> substrate. b, AFM image of a TaIrTe<sub>4</sub> flake. Inset exhibits the linecut profile, indicating a step thickness of approximately 0.8 nm. c, Raman spectrum of the TaIrTe<sub>4</sub> flakes ranging from 1L to 3L. With increasing layer numbers, the intensity ratio of  $A_2$  (@125.7 cm<sup>-1</sup> for 1L)/ $A_2$  (@137.3 cm<sup>-1</sup> for 1L) rises, and the  $A_1$  mode (@231.8 cm<sup>-1</sup> for 1L) shifts toward lower wavenumbers. d, Cross-sectional STEM images of monolayer, bilayer, and trilayer flakes.



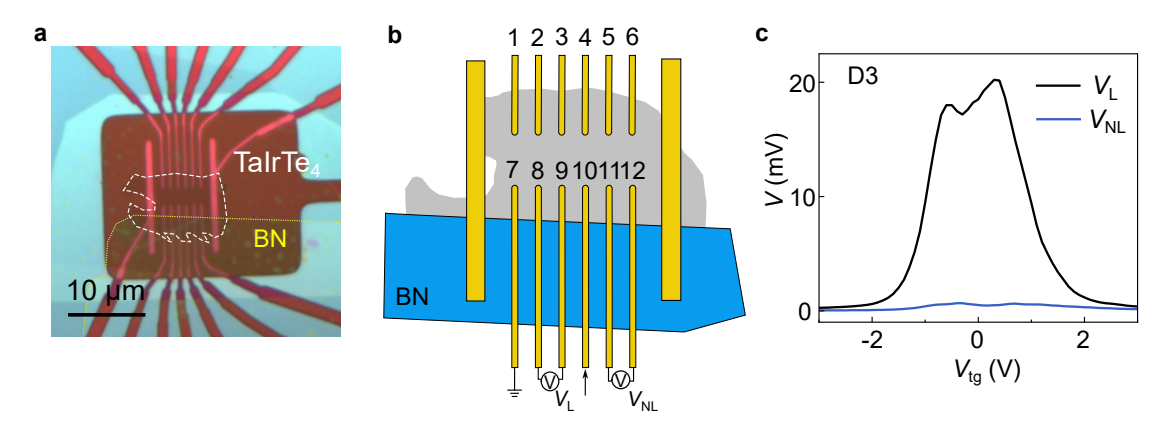
Extended Data Figure 2: Fabrication processes of TaIrTe<sub>4</sub> devices. a-b, Schematic and corresponding fabrication processes for Design-I (a) and Design-II (b) bottom structures. c, Fabrication processes of the top structure (involving TaIrTe<sub>4</sub> and top gate) conducted inside an argon-glovebox. Scale bars:  $10 \ \mu m$ .



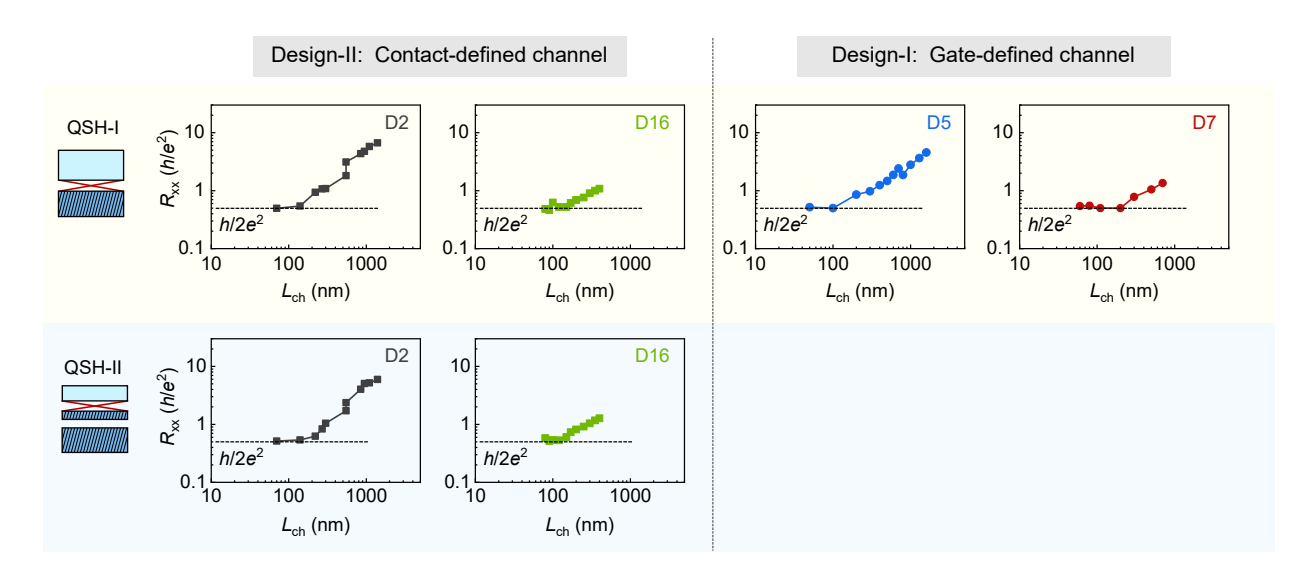
Extended Data Figure 3: Four-probe resistance versus carrier density and temperature. a, Device D17; b, Device D1; c, Device D2.



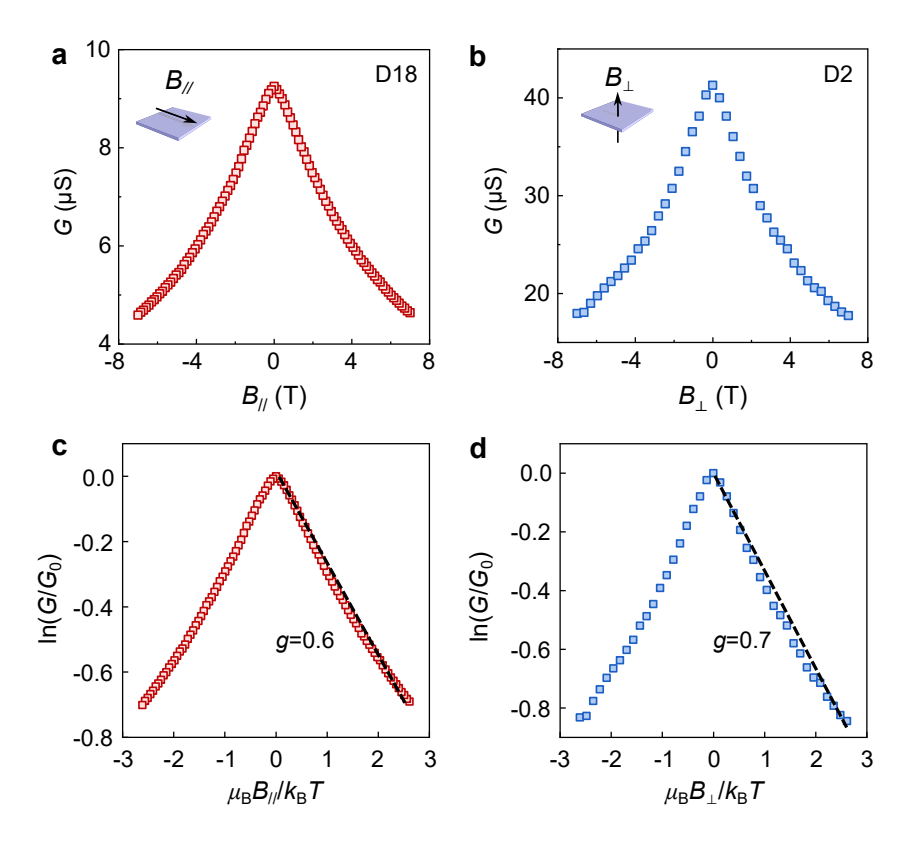
Extended Data Figure 4: Temperature dependence of CNP conductance and thermal activation fitting (device D2). The four-probe conductance ( $G_{xx}$ ) versus carrier density (n) is shown with temperatures ranging from 250 K to 4 K, along with corresponding thermal activation gap fits. Channel lengths: a-b,  $L_{ch}$ =220 nm, c-d,  $L_{ch}$ =270 nm, e-f,  $L_{ch}$ =550 nm, g-h,  $L_{ch}$ =850 nm, i-j,  $L_{ch}$ =950 nm, k-l,  $L_{ch}$ =1100 nm.



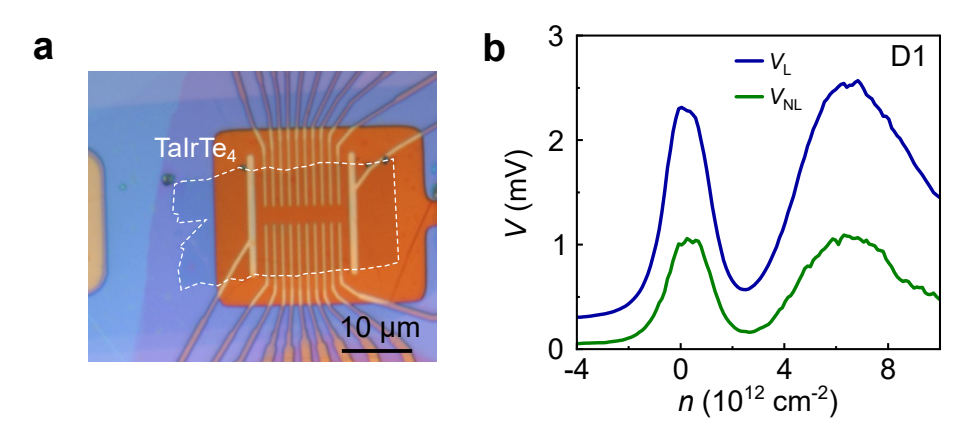
Extended Data Figure 5: Nonlocal measurements without edge contribution. a, An optical image of device D3 with half of its boundaries covered by BN. Scale bar: 10  $\mu$ m. b, Device schematic and contact labeling. c, Plots of local and nonlocal voltages versus carrier density n. The current was injected from Contact 10 to 7 ( $I_{xx} = 100 \text{ nA}$ ), and the voltages were measured between Contact 9 and 8 ( $V_L$ ) and between Contact 11 and 12 ( $V_{NL}$ ).



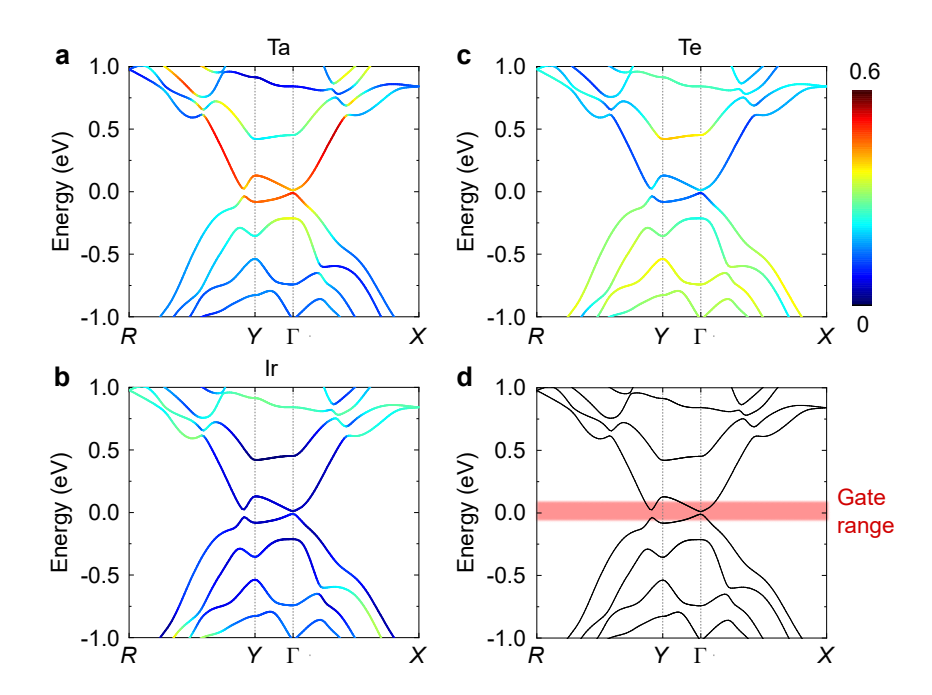
Extended Data Figure 6: Channel length dependence of the resistance at the CNP gap (QSH-I) as well as the correlated gap (QSH-II). Displayed here are the individual curves for devices D2, D5, D7, D16, as referenced in Fig. 2g and Fig. 4e.



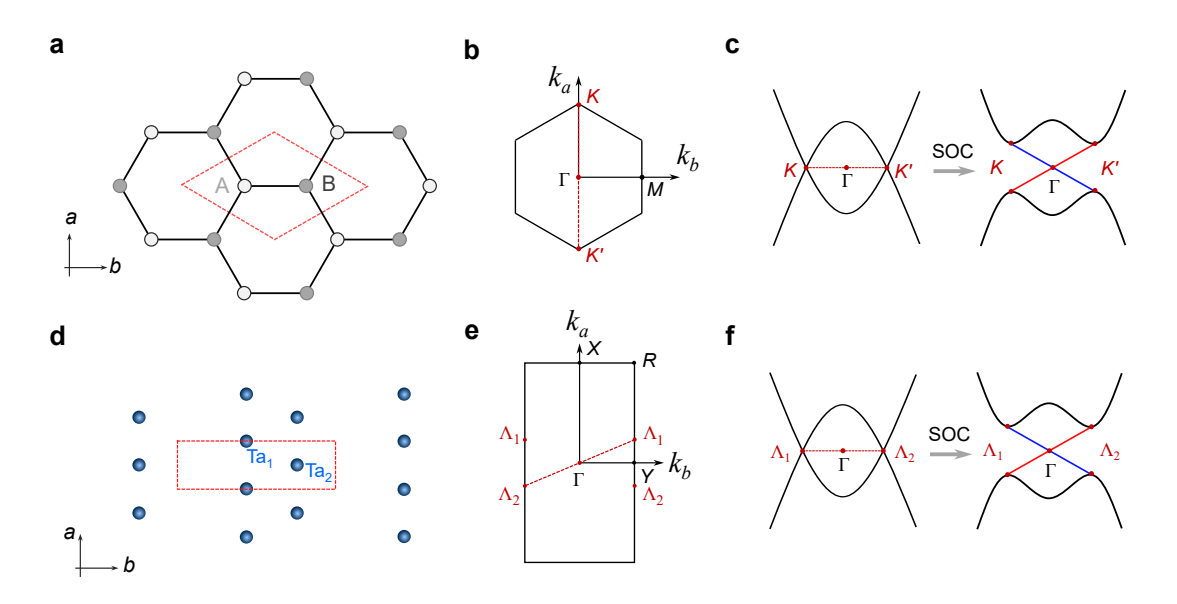
Extended Data Figure 7: Conductance at CNP under in-plane and out-of-plane magnetic fields. When a magnetic field is applied, a Zeeman gap is induced at the Dirac point of the edge states, influencing the edge conductance, which can be described by a thermal activation behavior:  $G = G_0 e^{-g\mu_{\rm B}|B|/2k_{\rm B}T}$ . Here,  $G_0$  is the conductance at B = 0, g is the effective g-factor,  $\mu_{\rm B}$  is the Bohr magneton, and  $k_{\rm B}$  is the Bohzmann constant. Panels (a-b) show the raw data G versus B for both in-plane and out-of-plane magnetic fields. Panels (c-d) plot the corresponding  $\ln(G/G_0)$  versus  $\mu_{\rm B}B/k_{\rm B}T$ , from the slope of which the g-factor can be directly extracted. The data was collected at T = 1.7 K.



Extended Data Figure 8: Enhanced nonlocal transport in both the CNP and second insulating gaps. a, An optical image of device D1. Scale bar: 10  $\mu$ m. b, The local  $(V_{\rm L})$  and nonlocal  $(V_{\rm NL})$  voltages measured with  $I_{\rm xx}=100$  nA.



Extended Data Figure 9: Band structure and its orbital decomposition for monolayer TaIrTe<sub>4</sub>. a-c, The orbital distribution of Ta (a), Ir (b) and Te (c), showing that the lowest energy bands originate primarily from Ta orbitals. d, The red-shaded region indicates the gate-tunable range within our experiment.



Extended Data Figure 10: Formation of QSH bands in TaIrTe<sub>4</sub>. a, Graphene lattice structure with two distinct atoms A and B per unit cell. b, Brillouin zone of graphene with K, K' and  $\Gamma$  points labeled. c, Existence of Dirac cones at K and K' points, where gap openings occur upon the introduction of spin-orbit coupling, leading to QSH edge states. d, Lattice structure of monolayer TaIrTe<sub>4</sub> with two distinct Ta atoms (Ta<sub>1</sub> and Ta<sub>2</sub>) within each unit cell. e, Brillouin zone of TaIrTe<sub>4</sub> with  $\Lambda_1$ ,  $\Lambda_2$ , and  $\Gamma$  points labeled. f, Existence of Dirac cones at  $\Lambda_1$  and  $\Lambda_2$  points, where gap openings occur due to spin-orbit coupling, leading to QSH edge states.